Research Square

Preprints are preliminary reports that have not undergone peer review.
They should not be considered conclusive, used to inform clinical practice,
or referenced by the media as validated information.

Comparative Assessment of 6/4, 8/6 and 10/8 Switched Reluctance Machines under Open-Circuit and Short-Circuit Phase Faults

SARA BARBARA

s.barbara@edu.umi.ac.ma

Universite Moulay Ismail De Meknes https://orcid.org/0009-0007-7636-8847

Research Article

Keywords: Switched reluctance machine, pole configuration, torque ripple, open-circuit fault, short-circuit fault, fault tolerance, MATLAB/Simulink

Posted Date: November 13th, 2026

DOI: https://doi.org/10.21203/rs.3.rs-11706067/v1

License: This work is licensed under a Creative Commons Attribution 4.0 International License.
Read Full License

Additional Declarations: The authors declare no competing interests.

Comparative Assessment of 6/4, 8/6 and 10/8 Switched Reluctance Machines under Open-Circuit and Short-Circuit Phase Faults

SARA BARBARA[1], Abdelmounim Dahane[1], Wissal touil[1], Adil Brouri[1]

[1] ENSAM, Moulay Ismail University, LMIMP laboratory, CSC teams, Morocco

Abstract

Switched Reluctance Motors (SRMs) have become a prominent choice in several applications due to their simplicity, high efficiency, and absence of permanent magnets or windings on the rotor. Additionally, they have superior fault tolerance, which allows them to continue to operate in the presence of faults. However, they are susceptible to defects and possible malfunctions that might have significant consequences for the system, the most common being short-circuit and open-circuit faults. This paper compares a three-phase 6/4, a four-phase 8/6 and a five-phase 10/8 SRM in MATLAB/Simulink, using the same asymmetric half-bridge converter, hysteresis current controller (30 A reference, 48 V DC link) and commutation angles, under healthy operation, a single-phase short circuit and a single-phase open circuit. Torque ripple, phase current and flux linkage are used as indicators. In the simulations, all three machines were able to continue operating under both faults. The study revealed that the pole and phase configuration influences how strongly faults affect the machine, with the 10/8 SRM showing the most favorable behavior among the three configurations under the studied conditions.

Keywords: *Switched reluctance machine; pole configuration; torque ripple; open-circuit fault; short-circuit fault; fault tolerance; MATLAB/Simulink*

1. Introduction

The adoption of electric vehicles (EVs) has increased significantly in recent decades driven by the need to reduce dependence on fossil fuels [1],[2]. This trend is shown by the expansion of the EV industry, which became remarkable, with their global which has become remarkable, with global electric car sales exceeding 20 million in 2025, about 20% more than in 2024 [3]. The electric motor is one of the crucial elements in the EV design, substantially influencing their performance, efficiency, and also dependability [4],[5]. Choosing a suitable motor requires considering several factors, including torque, power density, thermal behavior, and complexity associated with the control [6]. This choice can directly impact critical aspects of an EV, including its acceleration, range, and the driving experience [6]. Different types of electric motors are commonly used in EVs, each type has distinct advantages and drawbacks [1],[6]. For instance, permanent magnet synchronous motors (PMSMs) are known for their high efficiency, compact size, and their excellent torque characteristics, making them a popular choice in EV designs [7]. However, PMSMs rely on rare earth materials for their magnets, which can increase their cost and consequently raise concerns about the availability of the resource and environmental impact [7],[8]. On the other hand, induction motors, which are typically larger and heavier than PMSMs, offer benefits such as robustness and lower cost, and they do not require rare earth materials [9]. They have been widely used in EV traction drives due to their durability and reliability under various operating conditions [10]. However, the

presence of rotor windings increases maintenance requirements and reduces their reliability [9],[10]. Because of these drawbacks, researchers have looked for other motors that avoid rare earth magnets while staying reliable and low in cost. Switched reluctance motors (SRMs) are becoming attractive alternatives for EVs because of their simplicity, efficiency, and possible cost advantages [11],[12],[13]. SRMs do not require permanent magnets or rotor windings, unlike conventional motors, which reduces their reliance on costly rare-earth minerals [11],[12]. This not only reduces their costs but also enhances their durability and resilience [13]. Additionally, SRMs can continue to operate in the presence of certain faults [14],[15]. Furthermore, this type of machine can function at higher temperature conditions, which highlights a significant advantage in applications where thermal management is crucial [16]. These characteristics make SRMs a strong motor for electric vehicles, offering both cost and performance advantages while reducing reliance on critical materials. However, SRMs also have some drawbacks, mainly torque ripple [17],[18], and reduced performance under faults [19]. The ability of SRMs to function in fault conditions is a key feature that supports their use in EV applications. The inherent fault tolerance of SRMs, due to their phase independence, is widely documented [14],[15]. Fault behavior and diagnosis in SR drives have been studied for the classification and remediation of electrical faults [15], for winding short circuits [20] and for power-converter faults [21],[22]. In [23], the effect of open-phase faults on the noise and vibration of a 8/6 SRM was measured. A key study in [24] proposed a fault-tolerant converter topology for SRM drives, tested on three phase 12/8 and four phase 8/6 machines. This study demonstrated that even under open-circuit and short-circuit faults, the SRMs can continue to operate at reduced efficiencies. Fault diagnosis and fault-tolerant operation have also been studied for other EV drives, such as PMSMs [7], permanent magnet-assisted synchronous reluctance machines [26] and induction motors [27]. Although SRMs can keep running under faults, how well they run depends on torque ripple, which changes with the pole configuration. However, the authors in [28] show that the 6/4 configuration suffers from higher torque ripple than the 8/6 and 10/8 configurations. The reason is commonly attributed to fewer poles, which leads to irregular torque, and the torque ripple of doubly salient reluctance machines is known to depend on the phase number [29]. The torque ripple can also be influenced by the current; many studies have highlighted how varying current levels affect torque ripple in 8/6 SRMs [30],[31]. Additionally, the authors in [32] have shown that the shape and amplitude of the phase current are directly correlated with torque ripple characteristics. Then, they suggested that optimized current profiles can significantly reduce torque fluctuations.

Under faulty conditions, SRMs experience degradation in their performance, with phase losses and short-circuit faults leading to increased torque ripple and efficiency losses. Although they can continue to operate due to their separate phase excitation, SRMs with fewer phases, such as the 6/4, are expected to be more affected than the 8/6 and 10/8 SRMs, because each phase supplies a larger share of the torque. However, previous studies mostly deal with fault tolerance or torque ripple for a single configuration, and few compare the 6/4, 8/6, and 10/8 configurations under common converter and control settings. A recent study [33] compares 3-phase 6/4, 4-phase 8/6 and 5-phase 10/8 machines, but at different power ratings (75 kW for

the 4-phase machine and 10 kW for the 5-phase machine), so its results combine the effect of the pole configuration with that of the power rating. In this context, a comparison of the torque ripple, phase current and flux linkage of the 6/4, 8/6 and 10/8 SRM configurations is performed, which is one of the key contributions of this paper. This comparison is carried out with the same current reference (30 A) for the three machines. The same converter, hysteresis band and commutation angles are also used (except for the current band of the 10/8 open-circuit case, see Section 3.3); since the speed is not imposed, each machine settles at its own equilibrium speed, which is acknowledged as a limitation in Section 4. The simulated drives are small low-voltage drives (48 V DC link, 30 A current reference, speeds below 200 rpm); the EV context is therefore a motivation, and the results are relative comparisons between configurations rather than predictions for a traction drive. Table 1 summarizes the relevant literature on fault analysis and fault-tolerant operation in SRMs.

Table 1. Closest related studies and their relation to the present work.

Ref.	Machine(s)	Condition	Approach	Relation to this work
[15]	SR drive, general	Short and open circuits (winding, converter)	Review	this work adopts a single-phase short and open circuit
[21]	SR drive, asymmetric half-bridge converter	Open and short circuit of converter switches	Simulation and experiments; DC-bus current diagnosis	Fault detection only; this work quantifies the unmitigated effect of the faults
[23]	15 kW 8/6 SRM	Open phase	Experimental run-ups	Measured open-phase effect on noise and vibration (NVH); not directly comparable with the torque results here (Section 4)
[24]	3-phase 12/8, 4-phase 8/6	Open and short circuit	Simulation and experiments; fault-tolerant converter	Remedy-oriented; this work gives the unremedied baseline
[28]	6/4, 8/6, 10/8	Healthy	Multilevel-inverter simulation	Same three geometries; no faults
[33]	3-phase 6/4, 4-phase 8/6, 5-phase 10/8	Fault tolerance discussed	Comparative study at different power ratings	Same three geometries; not compared at a common power rating
[34]	SRM with parallel winding paths	Open and partial short circuit	Numerical	Winding-level influence; this work is topology-level
[35]	6/4, 8/6	Healthy	3-D finite elements	Field comparison; no faults
[36]	8/6, 10/8	Healthy	Validated analytical model	Modeling background; no faults
This work	6/4, 8/6, 10/8	Healthy, short, open	Simulink, same converter and controller, common current reference	Quantified comparison, analytical short-circuit bound, compensation estimate

The rest of this paper is organized as follows. Section 2 describes the SRM configurations, their modeling and the simulation setup. Section 3 presents the results. Section 4 discusses the findings, and Section 5 concludes the paper.

2. System Under Study and Modelling

2.1. Machine configurations

This paper investigates the impact of pole configuration on SRM performance during healthy and faulty operating conditions. Three different SRMs with different pole configurations, as depicted in Fig.1, are studied

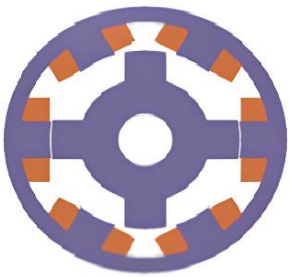


Fig. 1(a). 6/4 SRM.

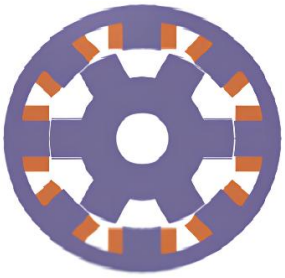


Fig. 1(b). 8/6 SRM.

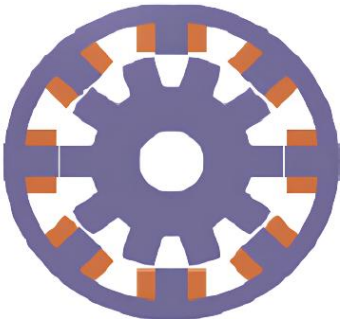


Fig. 1(c). 10/8 SRM.

Fig. 1. Cross-sections of the three SRMs studied.

Each machine is driven by an asymmetric half-bridge (AHB) converter, one leg per phase, so that the converter needs 6, 8 and 10 switches respectively. Phase commutation is derived from the rotor position, and the phase current is regulated by a hysteresis controller that keeps it inside a band around the reference (Fig. 2). The same converter type, the same controller and the same scenario definitions are used for all three machines.

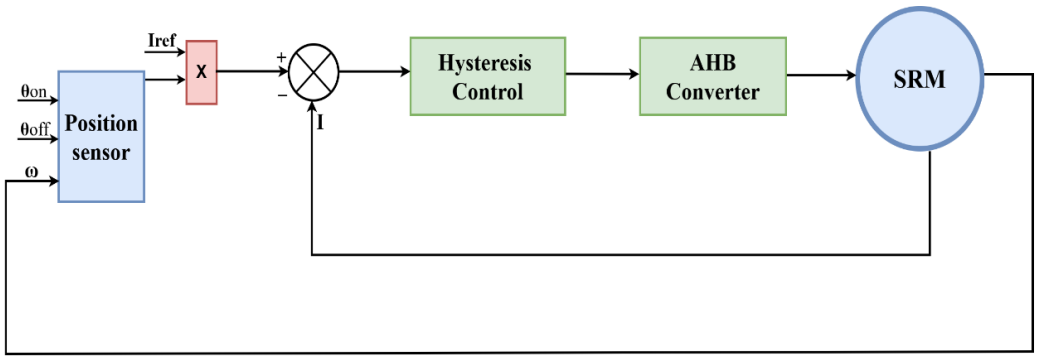


Fig. 2. Block diagram of the simulated drive: hysteresis current controller, asymmetric half-bridge converter, position sensor and SRM.

2.2. Mathematical model of the healthy machine

The model adopted in this study is illustrated in Fig.3. It contains the position-based commutation logic, the hysteresis current controller, the AHB converter and a nonlinear SRM block.

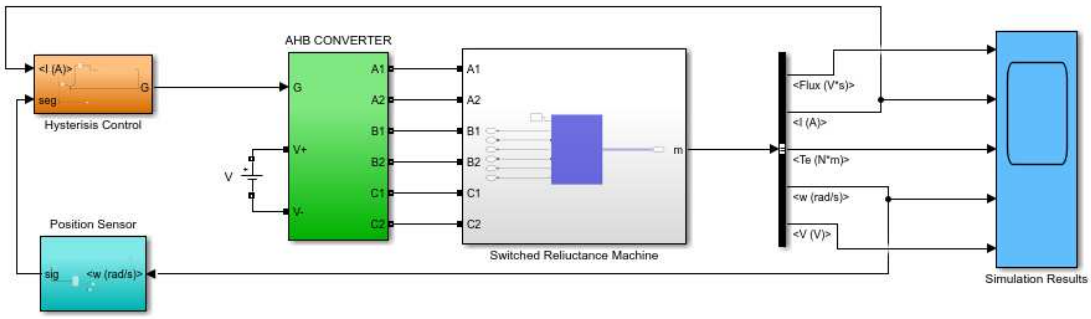


Fig. 3. Simulink model of the drive and the SRM.

For phase k, with resistance R, current i_k and flux linkage λ_k , the voltage expression for phase is derived from electromagnetic principles; it can be written as:

$$V_k(t) = Ri_k + \frac{d\lambda_k(t)(\theta,i)}{dt} \quad (1)$$

Where λ is the flux linkage per phase that can be expressed by:

$$\lambda_k(\theta,i) = L_k(\theta,i)i_k \quad (2)$$

We replace (2) in (1), and then the voltage can be expressed as:

$$V_k = Ri_k + L_k(\theta,i)\frac{di_k}{dt} + i_k\left(\frac{\partial L_k(\theta,i)}{\partial\theta}\omega + \frac{\partial L_k(\theta,i)}{\partial i_k}\frac{di_k}{dt}\right) \quad (3)$$

Where the induced back-electromotive force (back-emf) can be expressed as:

$$emf = i_k\frac{\partial L_k(\theta,i)}{\partial\theta}\omega \quad (4)$$

The inductance profile L(θ) of the SRM is an essential factor that influences its operation. The inductance varies with rotor position θ, as depicted in Fig. 4. Under healthy conditions, the inductance profile is periodic.

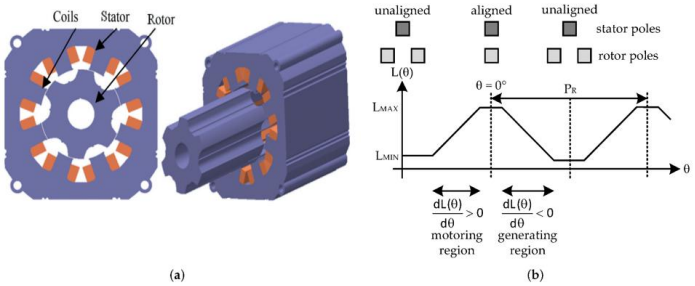


Fig. 4. Inductance profile of one phase of the SRM as a function of rotor position.

The produced torque is a function of the rotor position and the current, which is given by:

$$T_e = \frac{\partial W_c(\theta,i)}{\partial\theta}\Big|_{\text{i=cte}} \quad (5)$$

which reduces, for a magnetically linear circuit, to the familiar expression:

$$T_e = \frac{1}{2}\,i^2\,\frac{dL(\theta)}{d\theta} \quad (6)$$

While the mechanical equation involves the inertia J, the load torque T_L and the friction coefficient B:

$$J\frac{d\omega}{dt} = \frac{1}{2}i^2\frac{dL(\theta)}{d\theta} - T_L - B\omega \quad (7)$$

Eqs. (6) and (7) use the linear torque expression for illustration; the simulated SRM block accounts for the nonlinear magnetic characteristics.

The paper focuses on the performance characteristics analysis of three different configurations of SRMs; the 6/4, 8/6, and 10/8 designs. Each configuration presents distinct operational advantages and challenges, which influence both their suitability and applicability for specific applications.

2.3. Fault models

Two faults are applied to one phase (phase A) of each machine; a short circuit and an open circuit.

In the short-circuit case the faulted phase is still commutated at the nominal angles, but its current is no longer held at the 30 A reference, and the phase voltage is imposed by the converter. In the Simulink model, the short circuit is created by short-circuiting one phase of each machine. As shown by Eq. (9) below, the current of this phase is then limited only by the circuit and no longer by the 30 A reference, so it reaches about 10 to 13 times the reference current (Table 4), which is the expected behavior. The voltage balance of the faulted phase is therefore:

$$v_{ph} = R_{ph} i_{sc}(t) + \frac{d\lambda_{ph}}{dt} \tag{8}$$

Neglecting the saturation term, the current dynamics can be expressed as:

$$\frac{di_{sc}(t)}{dt} = \frac{v_{ph}}{L_{ph}(\theta)} - \frac{R_{ph}}{L_{ph}(\theta)} i_{sc}(t) - \frac{1}{L_{ph}(\theta)} \frac{\partial L_{ph}(\theta)}{\partial \theta} \omega i_{sc}(t) \tag{9}$$

Where v_{ph} is the voltage applied to the faulted phase by the converter, i_{sc} is the short-circuit current of a phase and $\omega = \frac{d\theta}{dt}$ is the rotor speed. Eq. (9) explains that the faulted-phase current is limited only by the resistance, the inductance and the motional term, which depends on $\frac{\partial L_{ph}(\theta)}{\partial \theta}$ and on the rotor speed ω ; with a 48V DC link and $R = 0.1\ \Omega$ it can therefore reach several hundred amperes.

When an open-circuit fault occurs in one phase, the behavior of the motor changes significantly. The current in that phase becomes zero. The fault in Simulink is created by inserting a very high resistance in series with the open phase. Consequently, the voltage for the open-circuited phase can be obtained from Eq. (1) by assuming the motor current to be zero as:

$$i_{ph}(t) = 0 \Rightarrow \lambda_{ph} \approx 0, V_{ph}(t) \approx 0 \tag{10}$$

The absence of current in the faulty phase directly influences the torque, since torque in SRMs strongly depends on phase current. This loss of current is expected to reduce the average torque and to increase the torque ripple; the ripple is quantified in Section 3.3. These fault conditions must be well understood to develop appropriate control strategies for improving the practical application reliability of SRMs.

2.4. Performance indicators

Torque ripple is the most frequently used indicator in this paper, so it is defined explicitly. Over one steady-state window of duration T, the average torque, the peak-to-peak torque and the torque ripple coefficient are defined as:

$$T_{avr} = \frac{1}{T}\int_0^T T_e(t)dt \tag{11}$$

$$T_{pp} = T_{max} - T_{min} \tag{12}$$

$$K_r = \frac{T_{max}-T_{min}}{T_{avr}} \tag{13}$$

The torque ripple coefficient K_r is the quantity to be compared with published values; it must always be quoted together with the operating speed and the current reference, because both change it strongly. In steady state, at constant average speed, the mean electromagnetic torque equals the load torque plus the friction torque, which is neglected here. Hence $T_{avr} = T_L$ when the speed is constant on average, and the same convention gives $K_r = \frac{T_{pp}}{T_L}$ in Tables 3 and 5. For the open-circuit cases it is applied to the late-run waveforms of Fig. 11, and the resulting values are indicative. During the short-circuit transient the speed is not constant, so no ripple coefficient is reported for it: Table 4 gives the peak current, the peak flux linkage, the peak torque and the duration of the transient instead. The severity of an open-circuit fault is also described by the relative change of the ripple coefficient:

$$\Delta K_r = \frac{K_{r,f} - K_{r,h}}{K_{r,h}} \tag{14}$$

where the subscripts h and f denote healthy and faulted operation. Because the torque dips of an open phase last for a rotor displacement rather than for a fixed time, the zero-torque interval is also expressed in mechanical degrees (interval × speed) and as a fraction of the stroke angle, which removes the effect of the operating speed on its duration. All indicators are read from the simulated waveforms, which is why approximate values are given in Tables 3 to 5.

Faults are applied to a single phase of each machine early in the simulation, before the drive has reached steady state (the faulted-phase torque response appears from about t ≈ 0.1 s in Fig. 8). The short-circuit fault is the phase-level fault defined in Section 2.3 and the open-circuit fault is an open winding, and both are permanent.

Because the short-circuit transients begin before steady state is reached, the reported durations and peak values include start-up effects and should be read as indicative; the open-circuit waveforms of Section 3.3 are taken late in the run (Fig. 11). The hysteresis current controller and the commutation angles are left unchanged after faults, so the results show the unmitigated effect of each fault.

2.5. Simulation setup

The simulation parameters are given in Table 2. The three machines are compared on the basis of an equal electrical excitation: the same DC-link voltage, converter, hysteresis current controller, current reference (30 A, ±10 A band) and commutation settings are used for all of

them, which gives the same electrical stress on the windings and on the converter. The speed and the output power are not imposed: each machine settles at its own operating point, determined by the torque it produces under this common current reference and by the load torque.

Table 2. Simulation parameters.

Parameter	**6/4**	**8/6**	**10/8**
DC-link voltage (V)	48	48	48
Phase resistance R (Ω)	0.1	0.1	0.1
Reference current / hysteresis band (A)	30 ± 10	30 ± 10	30 ± 10
Operating speed (rpm)	≈ 190	≈ 120	≈ 70
Load torque (N·m)	4.4	5.5	4.1
Inertia J (kg·m²)	0.01	0.01	0.01
Turn-off angle (°)	30	15	9
Turn-on angle (°)	0	0	0

3. Results

3.1. Healthy operation

Fig. 5 shows the electromagnetic torque of the three machines in steady state, and Table 3 lists the corresponding indicators. The 6/4 machine torque exhibits the highest torque ripple among the three configurations. While the 8/6 SRM, characterized by 8 stator poles and 6 rotor poles, gives a lower ripple coefficient (Kr ≈ 1.82 against ≈ 2.32), although its peak-to-peak torque is almost unchanged (≈ 10.0 against ≈ 10.2 N·m); the lower Kr is mainly due to the higher mean torque (5.5 against 4.4 N·m). The 10/8 machine has the lowest torque ripple of the three machines, in both peak-to-peak torque and ripple coefficient.

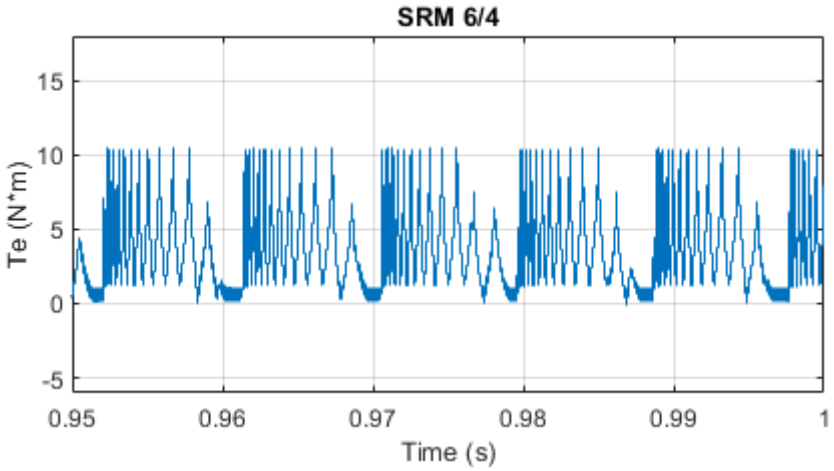


Fig. 5(a). Electromagnetic torque of the 6/4 SRM, healthy operation.

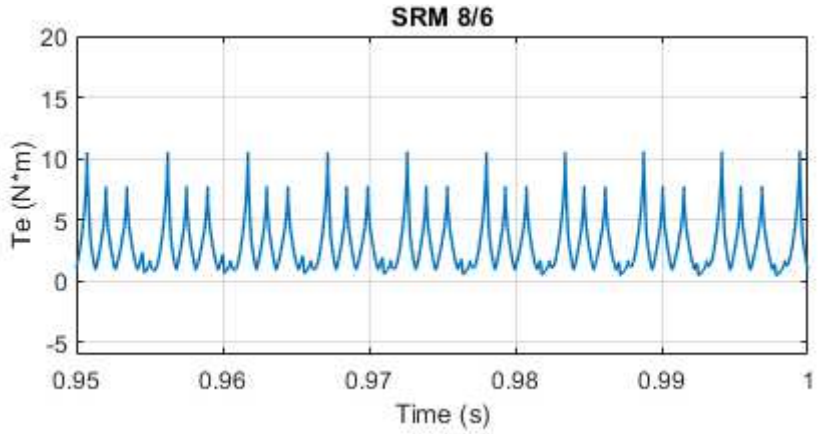


Fig. 5(b). Electromagnetic torque of the 8/6 SRM, healthy operation.

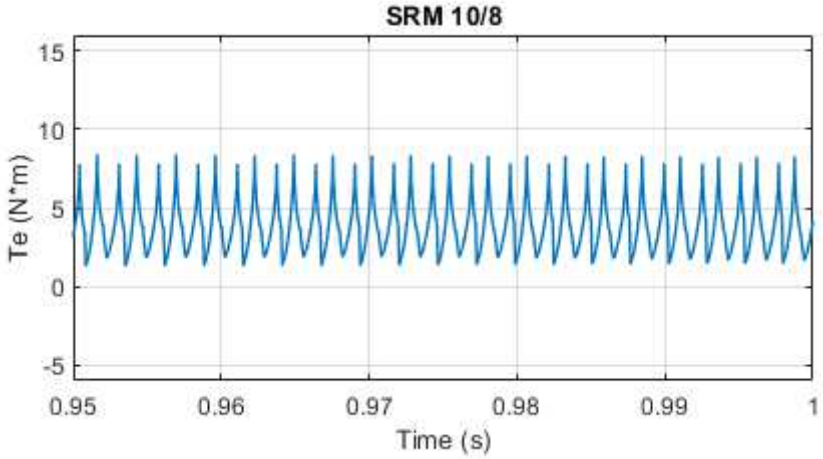


Fig. 5(c). Electromagnetic torque of the 10/8 SRM, healthy operation.

Fig. 6 compares the phase currents of the 6/4, 8/6, and 10/8 SRMs operating with the same converter type and current reference. The conduction time per stroke is about 26, 21 and 22 ms for the 6/4, 8/6 and 10/8 machines. These times are not a direct effect of the pole number: at the speeds of Table 2 (≈ 190, 120 and 70 rpm) they correspond to conduction angles of about 30°, 15° and 9°, that is, one stroke angle for each machine. In the 10/8 machine the current waveforms are distributed more evenly over the electrical cycle, and a slight overlap between consecutive phase currents is observed during commutation.

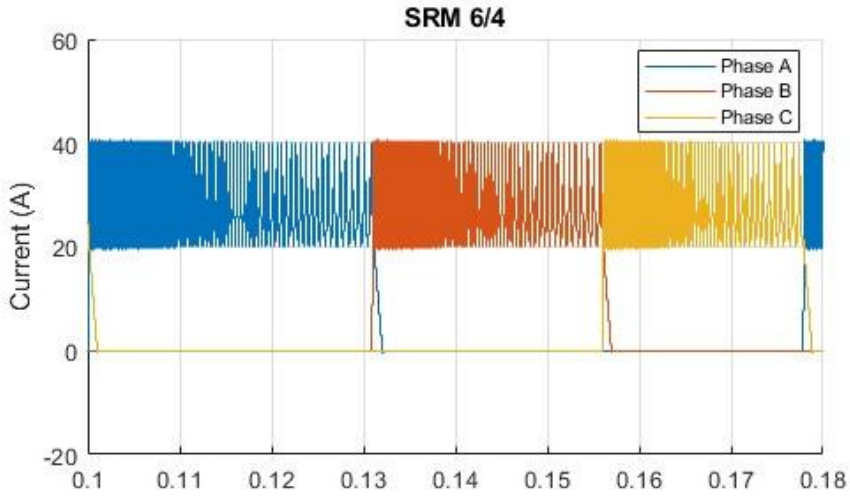


Fig. 6(a). Phase currents of the 6/4 SRM, healthy operation.

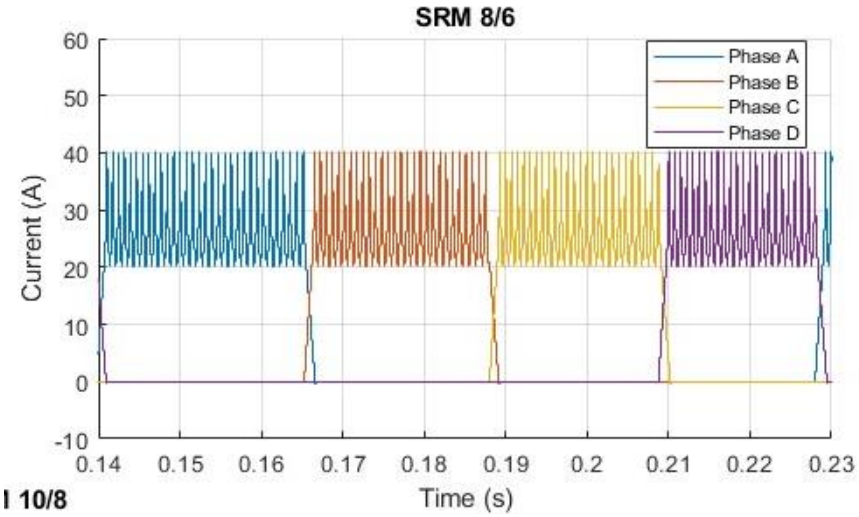


Fig. 6(b). Phase currents of the 8/6 SRM, healthy operation.

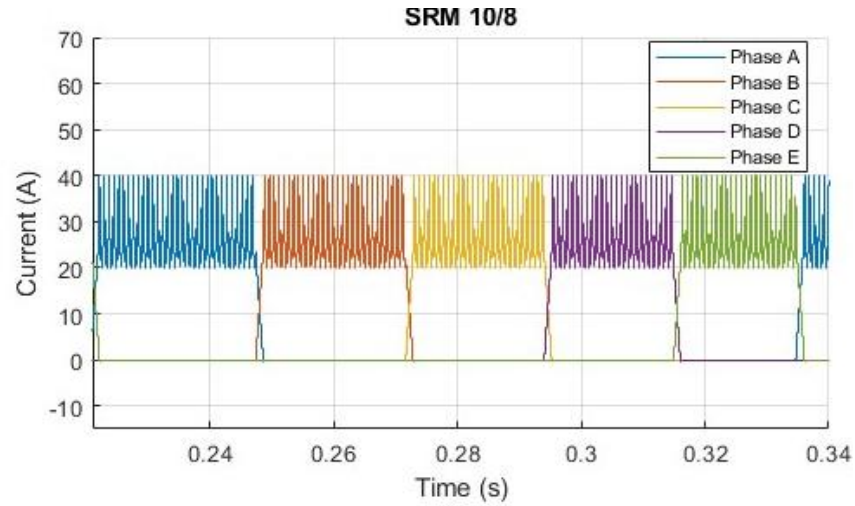


Fig. 6(c). Phase currents of the 10/8 SRM, healthy operation.

The flux waveforms show a behavior consistent with the current profiles presented in Fig.6. In the 6/4 machine, the flux rises almost linearly in each stroke to a peak of about 0.29 V·s and falls back to zero at commutation. In the 8/6 and 10/8 machines the flux is flatter and stays

between roughly 0.25 and 0.35 V·s during the conduction interval, with peaks of about 0.35 V·s, which is about 21% higher than in the 6/4 machine. The higher peak flux of the machines with more phases means that their individual phases work at a higher magnetic loading than the 6/4 phase in this simulation, where the speed is also different.

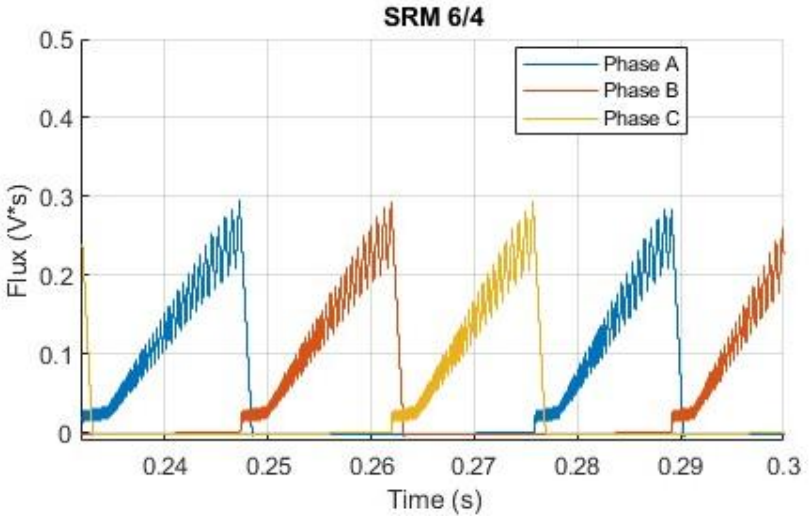


Fig. 7(a). Flux linkage of the 6/4 SRM, healthy operation.

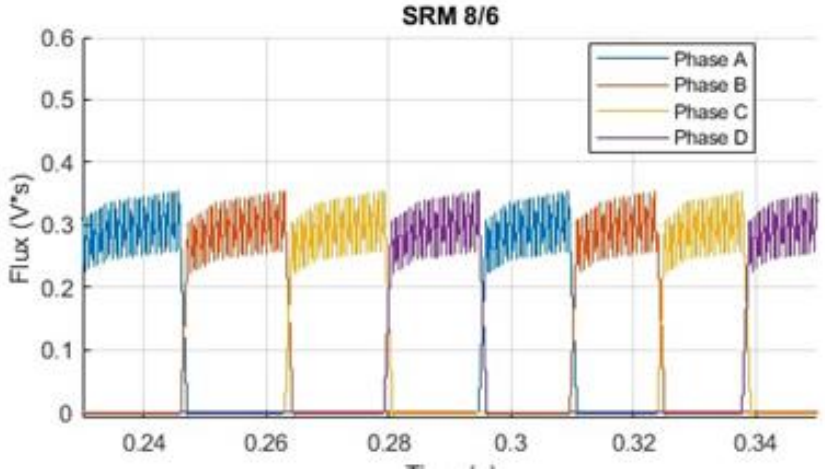


Fig. 7(b). Flux linkage of the 8/6 SRM, healthy operation.

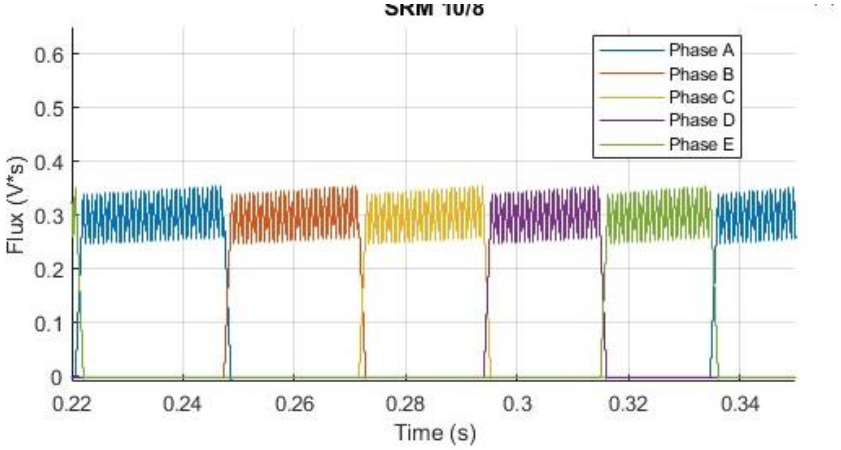


Fig. 7(c). Flux linkage of the 10/8 SRM, healthy operation.

Table 3. Indicators for healthy operation

Indicator	**6/4**	**8/6**	**10/8**
Torque range $T_{min} - T_{max}$ $(N \cdot m)$	≈ 0.3–10.5	≈ 0.5–10.5	≈ 1.3–8.3
Peak-to-peak torque T_{pp} (N·m)	≈ 10.2	≈ 10.0	≈ 7.0
Ripple coefficient K_r	≈ 2.32	≈ 1.82	≈ 1.71
Current band (A)	≈ 20–40	≈ 20–40	≈ 20–40
Conduction time per stroke (ms)	≈ 26	≈ 21	≈ 22
Peak flux linkage (V·s)	≈ 0.29	≈ 0.35	≈ 0.35

3.2. Single-phase short-circuit fault

Fig. 8 shows the torque response with one phase short-circuited, and Table 4 lists the indicators. In all three machines the torque before the fault (insets of Fig. 8, up to about 100 N·m) still reflects the start-up of the drive and is about ten times the ≈ 10 N·m of healthy steady state (Fig. 5). When the fault acts, the torque rises sharply and reaches peaks of about 7300, 8200 and 10800 N·m for the 6/4, 8/6 and 10/8 machines respectively (Table 4), far above the roughly 10 N·m of healthy operation. These values are results of the model for a permanent, unmitigated fault with currents far above the 30 A regulated level; a real drive would be protected within milliseconds, so they should not be read as torques that a real machine would deliver and are used only to compare the relative severity of the fault between the three machines. The transient lasts about 31 ms in the 6/4 machine and about 30 ms in the 8/6 machine, against about 18 ms in the 10/8 machine, which is about 40% shorter.

Under a short circuit the 10/8 machine therefore shows the shortest disturbance in these simulations, but also the highest peak torque, whereas the 6/4 and 8/6 machines differ little in duration; the shorter duration should be confirmed with the same fault instant for all machines.

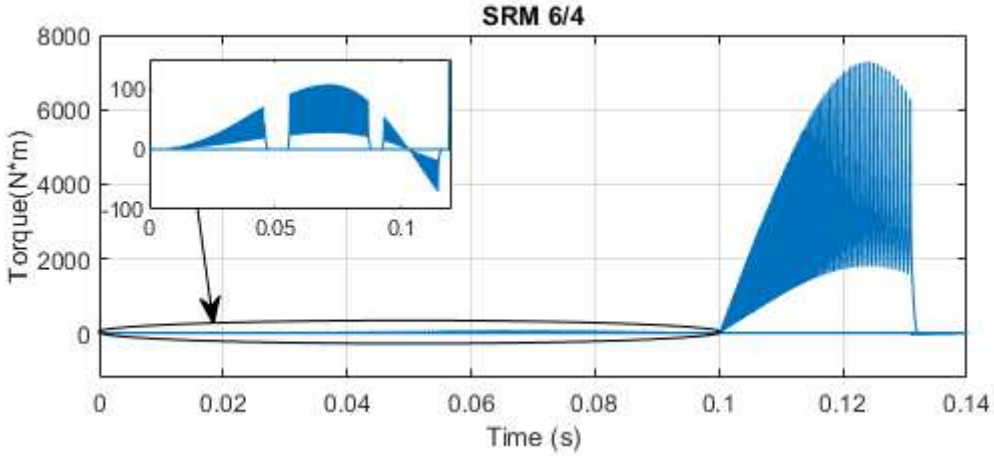


Fig. 8(a). Electromagnetic torque of the 6/4 SRM, single-phase short circuit.

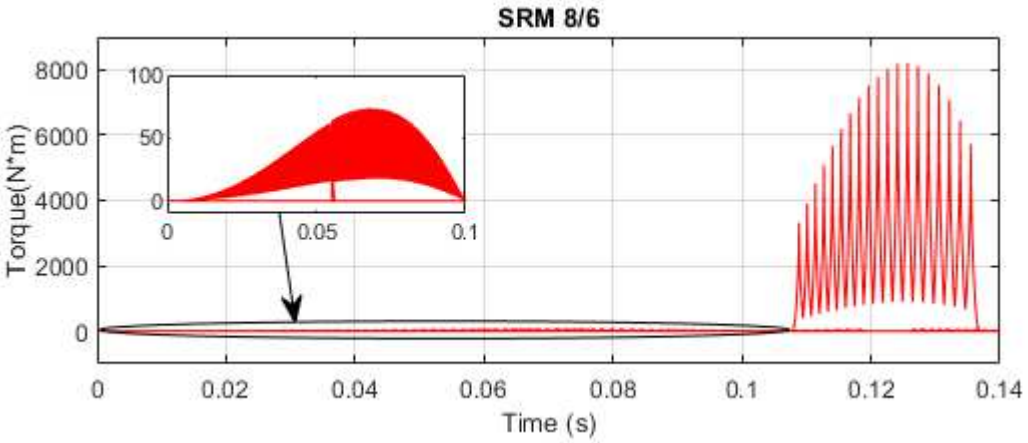


Fig. 8(b). Electromagnetic torque of the 8/6 SRM, single-phase short circuit.

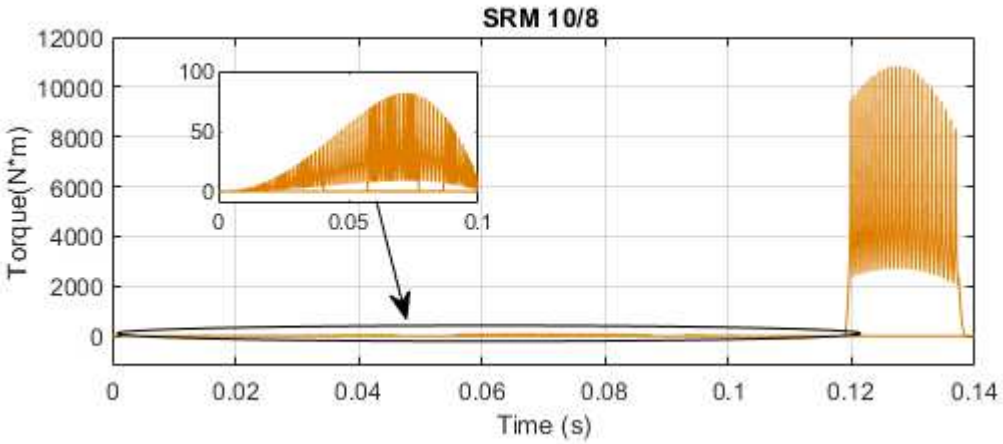


Fig. 8(c). Electromagnetic torque of the 10/8 SRM, single-phase short circuit.

The faulted-phase current rises far above the regulated level depicted in Fig. 9. In the 6/4 and 8/6 machines, it reaches about 400 A, oscillating between roughly 200 and 400 A, whereas in the 10/8 machine it peaks at about 300 A, between roughly 100 and 300 A. The peak fault current of the 10/8 machine is thus about 25% lower than that of the other two, although it is still about ten times the 30 A reference. Since the motional term in Eq. (9) is proportional to

the rotor speed and its effect depends on the rotor position, the difference between the machines cannot be attributed to the pole configuration alone: the three machines run at different speeds (≈ 190, 120 and 70 rpm). The 8/6 machine does not limit the peak current below that of the 6/4 machine, and shows no clear advantage over it under a short circuit. The healthy phases stay near the regulated band in all three machines.

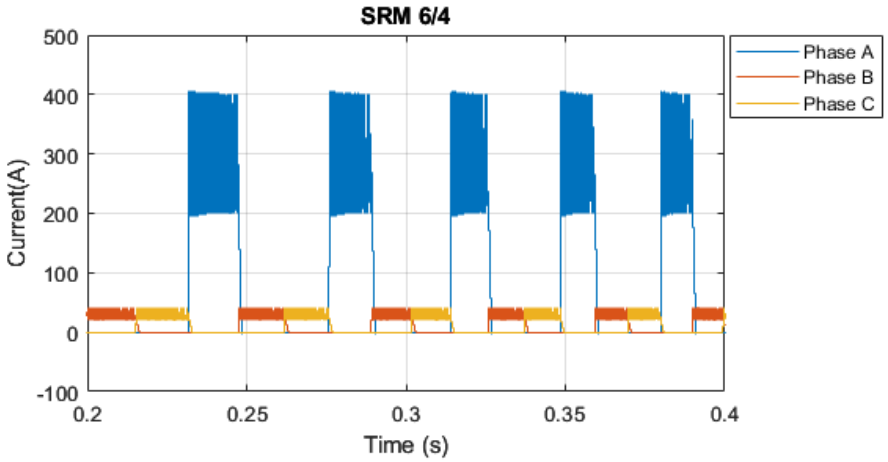


Fig. 9(a). Phase currents of the 6/4 SRM, single-phase short circuit.

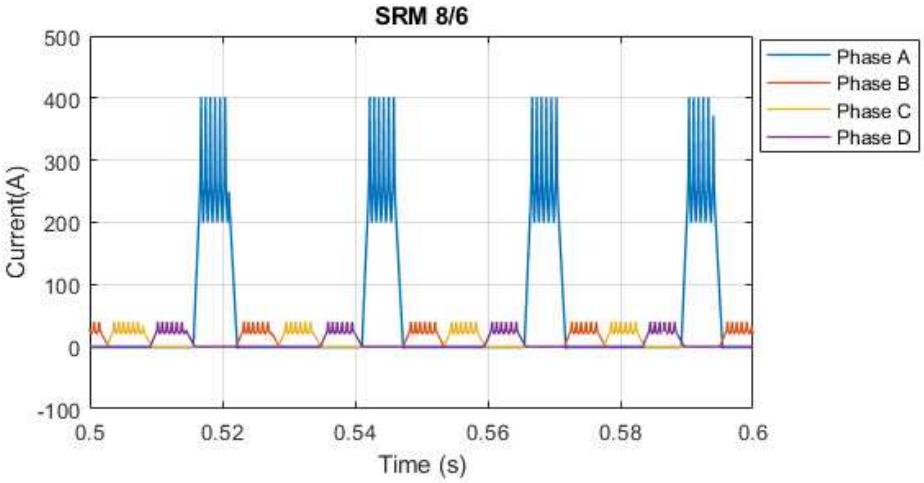


Fig. 9(b). Phase currents of the 8/6 SRM, single-phase short circuit.

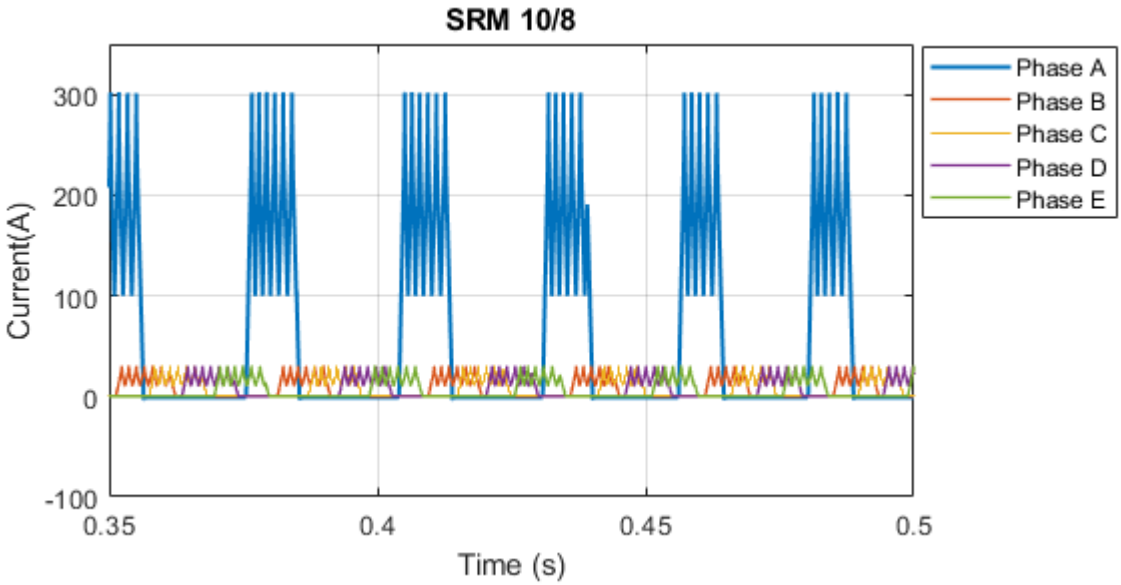


Fig. 9(c). Phase currents of the 10/8 SRM, single-phase short circuit.

The flux linkage shown in Fig. 10 reveals the magnetic consequence of the fault. The faulted phase reaches a peak of about 0.45 V·s in the 6/4 machine, 0.50 V·s in the 8/6 machine and 0.48 V·s in the 10/8 machine. Compared with the healthy peaks which are about 0.29, 0.35 and 0.35 V·s, this is an increase of about 55%, 43% and 37%, so the 6/4 phase is the one whose magnetic loading rises most in relative terms, although its absolute peak is the lowest of the three. Among the machines, the 8/6 peak is about 11% above the 6/4 and the 10/8 peak about 7% above it and about 4% below the 8/6. The flux waveform of the 10/8 machine is also the most crowded, since its phases overlap the most.

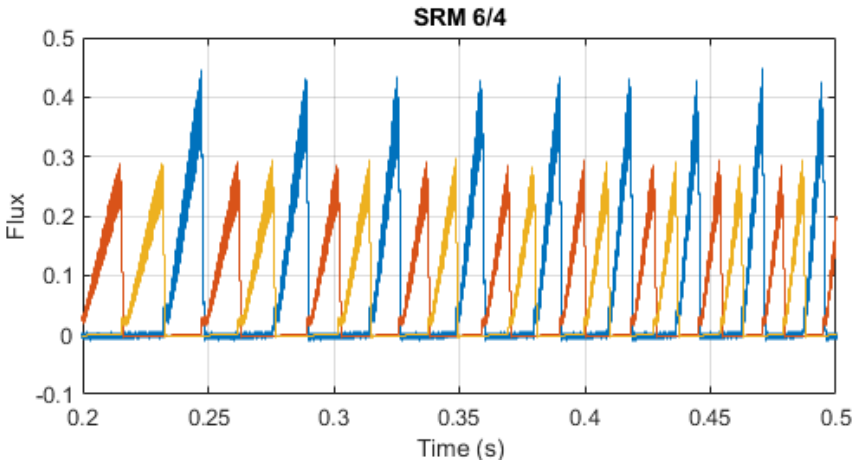


Fig. 10(a). Flux linkage of the 6/4 SRM, single-phase short circuit.

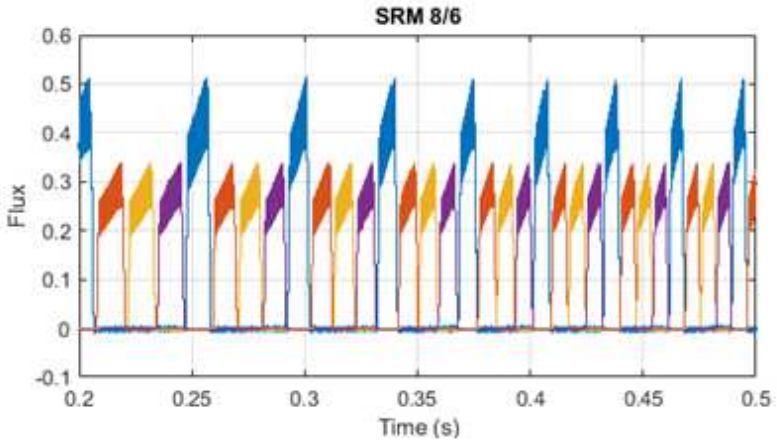


Fig. 10(b). Flux linkage of the 8/6 SRM, single-phase short circuit.

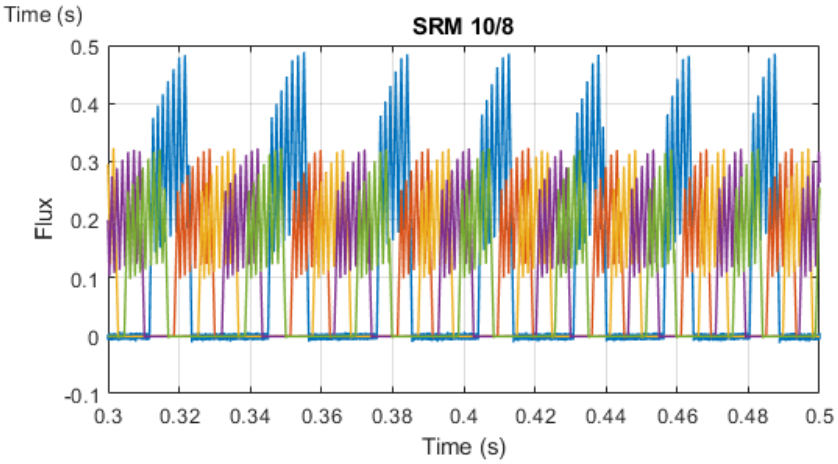


Fig. 10(c). Flux linkage of the 10/8 SRM, single-phase short circuit.

Table 4. Indicators under a single-phase short circuit

Indicator	**6/4**	**8/6**	**10/8**
Peak faulted-phase current (A)	≈ 400	≈ 400	≈ 300
Peak current / reference (30 A)	≈ 13.3	≈ 13.3	≈ 10.0
Peak flux linkage (V·s)	≈ 0.45	≈ 0.50	≈ 0.48
Peak flux relative to healthy case (%)	≈ +55	≈ +43	≈ +37
Current range of faulted phase (A)	≈ 200–400	≈ 200–400	≈ 100–300
Duration of the torque transient (ms)	≈ 31	≈ 30	≈ 18
Peak torque during the transient (N·m)	≈ 7300	≈ 8200	≈ 10800

3.3. Single-phase open-circuit fault

When one phase is open, the torque of every machine drops to about zero during the part of the cycle in which the faulted phase should have produced it as presented in Fig. 11. In the 6/4 machine these intervals are the longest, lasting about 12 to 14ms, and the torque even becomes slightly negative at one point. In the 8/6 machine they are shorter, about 6 to 10ms, and in the 10/8 machine they appear as brief dips of about 2 to 5ms, because the neighboring phases partly

cover the missing stroke. This follows the share of excitation that is lost, one phase out of three, four and five, which is about 33%, 25% and 20% respectively (Table 5). The peak torque stays near the healthy level in all machines about 10.5 for 6/4 SRM, 10.5 for 8/6 SRM and for 10/8 SRM about 8.5N·m. The peak-to-peak torque increases from about 10.2 to 11.5 N·m in the 6/4 machine that is about +13%, from 10.0 to 10.5 N·m in the 8/6 machine which is about +5% and from 7.0 to 8.5 N·m in the 10/8 machine that is about +21%. In absolute terms the 10/8 machine keeps the lowest peak-to-peak torque, about 19% below the 8/6 and 26% below the 6/4.

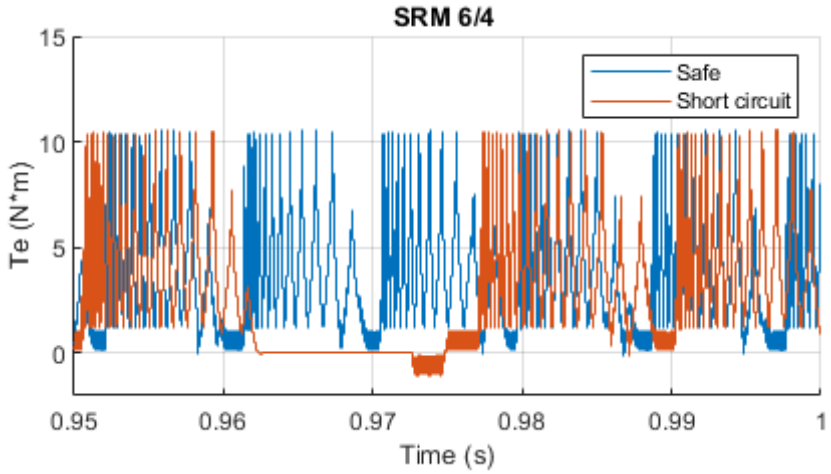


Fig. 11(a). Electromagnetic torque of the 6/4 SRM, healthy and single-phase open circuit.

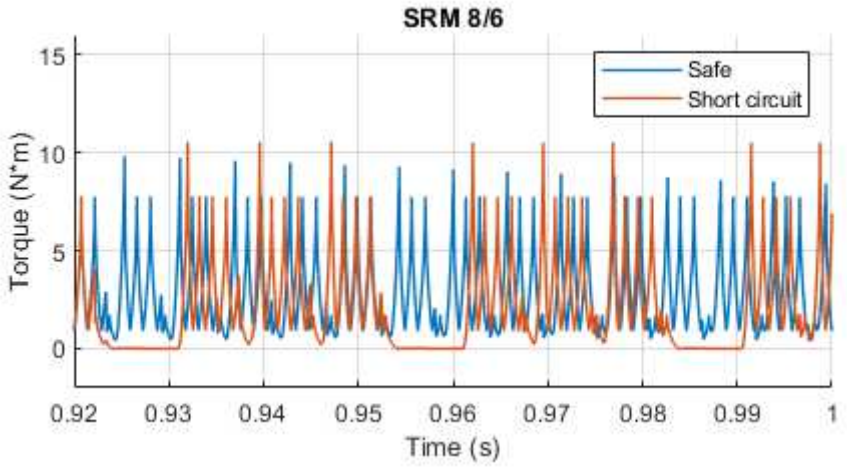


Fig. 11(b). Electromagnetic torque of the 8/6 SRM, healthy and single-phase open circuit.

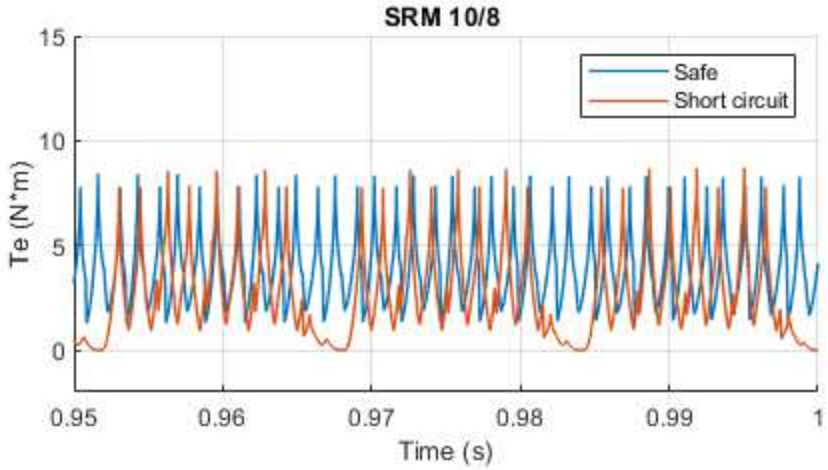


Fig. 11(c). Electromagnetic torque of the 10/8 SRM, healthy and single-phase open circuit.

The remaining phases carry the load shown in Fig.12. The 6/4 and 8/6 machines run with peak currents of about 40 A, and the 10/8 machine with about 30 A, that is, about 25% lower. However, in the 10/8 machine the current is regulated between about 10 and 30 A in this case, against 20–40 A in the healthy case, so the lower peak is due to a lower current band and cannot be attributed to the larger number of phases. The open-circuit results of the 10/8 machine are therefore not obtained with exactly the same current reference as for the other two machines. In the 6/4 machine only two phases remain to produce torque, and each conduct for a long interval. With three and four remaining phases in the 8/6 and 10/8 machines, the load is shared among more phases, and the average share of the load per remaining phase decreases from about 50% to about 33% and 25%, with correspondingly shorter conduction intervals.

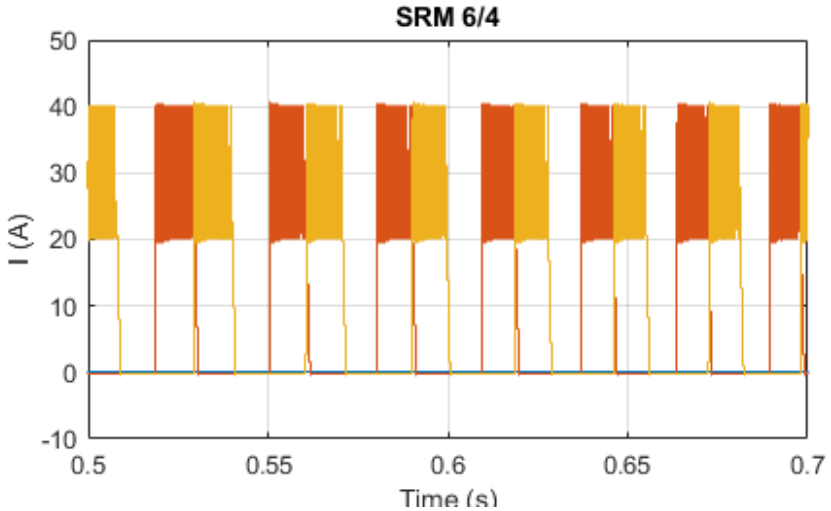


Fig. 12(a). Phase currents of the 6/4 SRM, single-phase open circuit.

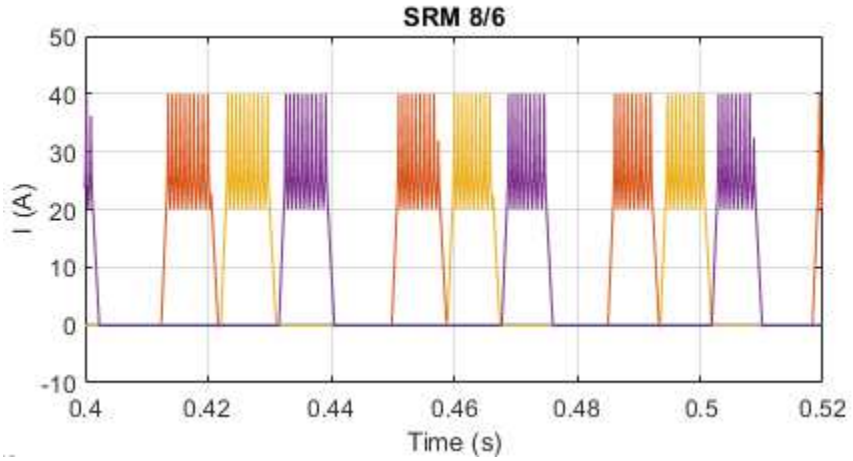


Fig. 12(b). Phase currents of the 8/6 SRM, single-phase open circuit.

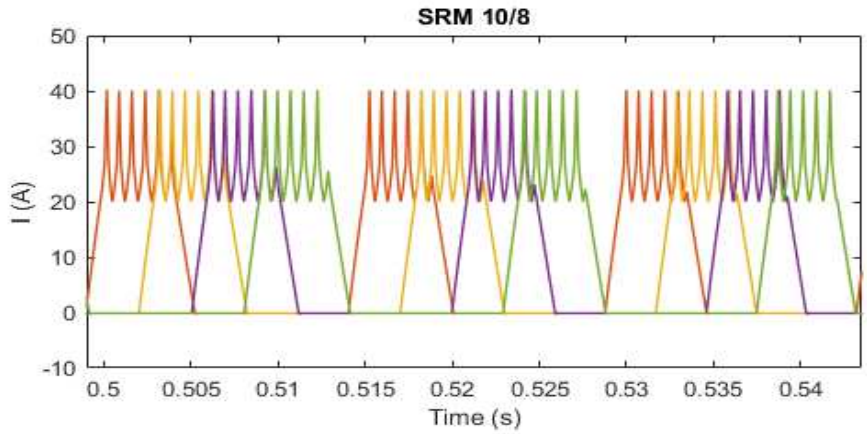


Fig. 12(c). Phase currents of the 10/8 SRM, single-phase open circuit.

The flux linkage presented in Fig. 13 has no contribution from the open phase, as expected. In the 6/4 machine the remaining flux profiles are separated by wide gaps, with peaks of about 0.29 V·s, equal to the healthy value. The 8/6 machine reaches peaks of about 0.33 V·s with shorter gaps, that is about 14% above the 6/4 and about 6% below its healthy peak. The 10/8 machine reaches about 0.32 V·s, about 10% above the 6/4 and about 9% below its healthy peak, with flux profiles that overlap almost continuously. The peak values do not differ much among the machines, and the benefit of additional phases appears in the continuity of the magnetic loading rather than in its magnitude.

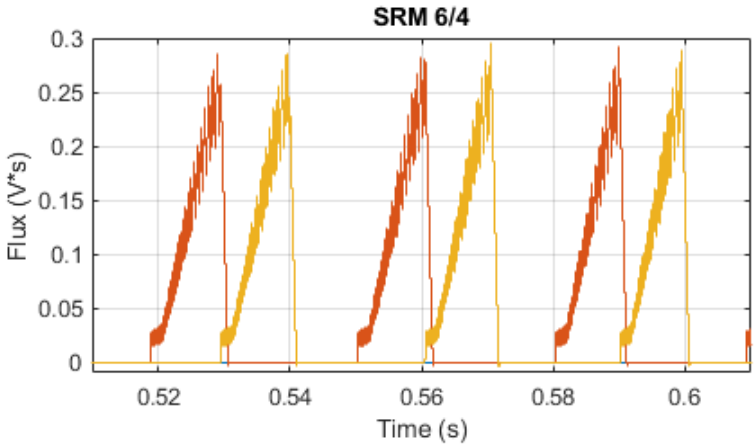


Fig. 13(a). Flux linkage of the 6/4 SRM, single-phase open circuit.

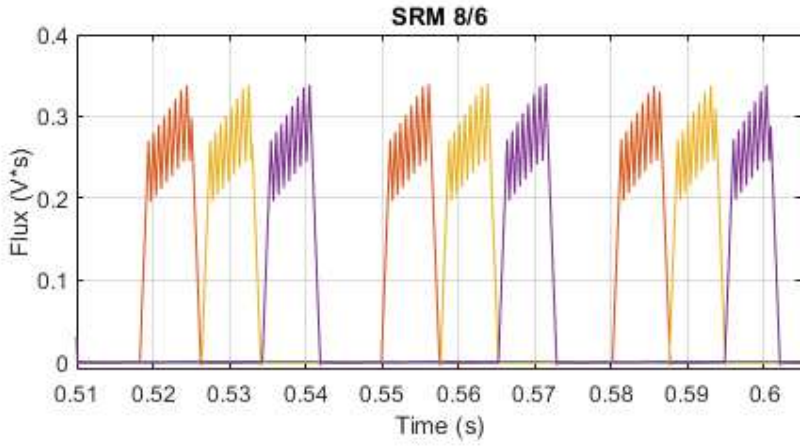


Fig. 13(b). Flux linkage of the 8/6 SRM, single-phase open circuit.

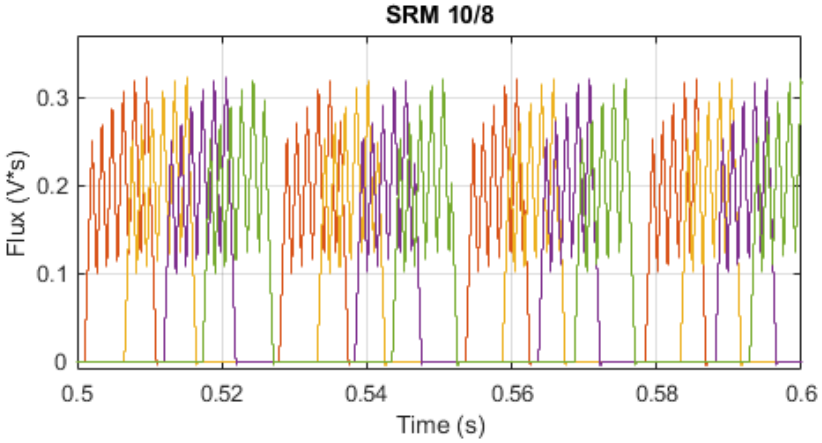


Fig. 13(c). Flux linkage of the 10/8 SRM, single-phase open circuit.

Table 5. Indicators under a single-phase open circuit

Indicator	6/4	8/6	10/8
Fraction of phases lost (%)	33	25	20
Zero-torque interval of the faulted stroke (ms)	≈ 12–14	≈ 6–10	≈ 2–5
Peak flux linkage (V·s)	≈ 0.29	≈ 0.33	≈ 0.32
Peak-to-peak torque (N·m)	≈ 11.5	≈ 10.5	≈ 8.5
Peak Torque (N.m)	≈ 10.5	≈ 10.5	≈ 8.5
Ripple coefficient K_r	≈ 2.61	≈ 1.91	≈ 2.07

4. Discussion

In all scenarios the three machines kept running, which is consistent with the inherent fault tolerance expected from phase independence [14],[15]; the degradation differs between the configurations but does not decrease monotonically with the number of phases. The 10/8 machine has the lowest ripple in healthy operation (Kr ≈ 1.71 against ≈2.32 for the 6/4). Under a short circuit it has the shortest torque transient and the lowest fault current (≈ 18 ms and ≈ 300 A against ≈ 30–31 ms and ≈ 400 A). However, its peak torque during the transient is the highest (≈ 10800 N·m against ≈ 7300 and ≈ 8200 N·m). Under an open circuit it has the shortest zero-torque dips (≈ 2–5 ms against ≈ 12–14 ms). This is consistent with the lost phase representing only 20% of the excitation instead of 33%, and with the neighboring phases partly covering the missing stroke, but with the present set-up this explanation cannot be separated from the effect of speed, load and current band. The advantage is not uniform, however. Under an open circuit the relative increase of ripple is largest for the 10/8 machine (+21% against +5% for the 8/6), and under an open circuit its ripple coefficient (≈ 2.07) is also higher than that of the 8/6 machine (≈ 1.91, Table 5). The 10/8 open-circuit case was also run with a lower current band (≈ 10–30 A) than the healthy case (≈ 20–40 A), and its Kr, like the others in Table 5, is computed with the load torque as the mean torque, so the open-circuit ripple comparison should be regarded as indicative only. The results also combine the effect of pole and phase count with that of different operating speeds (≈ 190, 120 and 70 rpm), and load torques (Table 2), which correspond to different output powers (about 90 W, 70 W and 30 W, calculated as load torque times speed). The speed is not imposed in the model: it results from the balance between the torque produced under the same current reference and the load torque, so it could not be equalized without changing the current reference or the load. A comparison at equal speed is therefore left for future work. Differences of a few percent, such as between the healthy ripple coefficients of the 8/6 and 10/8 machines (≈ 1.82 and ≈ 1.71) or between the flux peaks, are within the accuracy with which values are read from the waveforms and are not a basis for ranking the machines. They come from a simulation-only study with idealized faults, and the extra converter complexity of the 10/8 (10 switches against 6) is not quantified. The open-phase results cannot be compared quantitatively with the measurements in [23], which report noise and vibration orders during run-ups of a 15 kW machine rather than torque dips; the two studies are consistent only in that an open phase degrades the operation of the machine. The unremedied degradation found here is the situation that the fault-tolerant topology of [24] and the control strategies of [15] aim to correct.

5. Conclusions

This paper compared a three-phase 6/4, a four-phase 8/6 and a five-phase 10/8 SRM under healthy operation, a single-phase short circuit and a single-phase open circuit, using the same converter and controller. In the simulations, all three machines continued to operate under both faults, which is consistent with the fault tolerance expected from the independence of the phases. The study is a comparison and not an optimization. Its main quantitative findings are as follows.

In healthy operation, the peak-to-peak torque is about 7 N·m for the 10/8 machine and about 10 N·m for the 6/4 and 8/6 machines, and the ripple coefficient of the 10/8 machine (≈ 1.71) is about 26% below that of the 6/4 machine (≈ 2.32) and about 6% below that of the 8/6 machine (≈ 1.82). Under a short circuit, the peak faulted-phase current is about 300 A for the 10/8 machine against about 400 A for the other two, and its torque transient is about 40% shorter (≈ 18 ms against ≈ 30–31 ms). Under an open circuit, the ripple coefficient of the 10/8 machine (≈ 2.07) is about 21% below that of the 6/4 machine (≈ 2.61) but about 8% above that of the 8/6 machine (≈ 1.91), so its main benefit is a reduction of the zero-torque dips (≈ 2–5 ms against ≈ 12–14 ms). All three machines remained operational in all scenarios.

These findings are limited by the simulation-only approach, by the entanglement of pole count and phase count, and by the open points listed in Section 4. Future work should (i) validate the results on a finite-element model and on a test bench, (ii) compare the machines at the same speed (by adjusting the load torque of each machine or by imposing the speed), the same power rating and the same current reference, and compare the ripple coefficient with published values, (iii) separate pole count from phase count, (iv) design and test fault-tolerant control strategies, including current redistribution among the healthy phases, and (v) assess thermal behavior and efficiency under fault.

Acknowledgment:

The corresponding author would like to express their sincere gratitude to the **National Center for Scientific and Technical Research (CNRST)** for its valuable support.

References

[1] Krishnamoorthy, S., & Panikkar, P. P. K. (2024). A comprehensive review of different electric motors for electric vehicles application. *International Journal of Power Electronics and Drive Systems*, *15*(1), 74–90. https://doi.org/10.11591/ijpeds.v15.i1.pp74-90

[2] Dahane, A., Mansouri, F. E., Barbara, S., Hjjouji, A., Kabassi, I. E., & Brouri, A. (2026). Multi-objective design optimization and performance assessment of an 8/6 switched reluctance machine for electric propulsion applications. *IEEE Access*, *14*, 88009–88024. https://doi.org/10.1109/access.2026.3701845

[3] International Energy Agency. (2026). Global EV Outlook 2026. IEA, Paris, France. https://www.iea.org/reports/global-ev-outlook-2026

[4] Saleh, A. L., Al-Amyal, F., & Számel, L. (2024). Control techniques of switched reluctance motors in electric vehicle applications: A review on torque ripple reduction strategies. *AIMS Electronics and Electrical Engineering*, *8*(1), 104–145. https://doi.org/10.3934/electreng.2024005

[5] Lan, Y., Benomar, Y., Deepak, K., Aksoz, A., Baghdadi, M. E., Bostanci, E., & Hegazy, O. (2021). Switched reluctance motors and drive systems for electric vehicle powertrains: State of the art analysis and future trends. *Energies*, *14*(8), 2079. https://doi.org/10.3390/en14082079

[6] Zhu, Z. Q., & Howe, D. (2007). Electrical machines and drives for electric, hybrid, and fuel cell vehicles. *Proceedings of the IEEE*, *95*(4), 746–765. https://doi.org/10.1109/jproc.2006.892482

[7] Lin, Z. Y., Liu, Z. S., & Chen, P. Y. (2025b). Design and analysis of permanent magnet synchronous motor for electric vehicle. *Journal of Physics Conference Series*, *3144*(1), 012009. https://doi.org/10.1088/1742-6596/3144/1/012009

[8] Kumar, K., Vaiyapuri, V., & Nadarajan, S. (2025). Permanent magnet synchronous motor faults detection using current harmonics and K-Means clustering. *IEEE Journal of Emerging and Selected Topics in Industrial Electronics*, *7*(1), 13–23. https://doi.org/10.1109/jestie.2025.3609657

[9] Lumyong, P., & Sarikprueck, P. (2018). A study on Induction Motor Efficiency Improvement for Implementing in Electric Vehicle. *International Conference on Electrical Machines and Systems (ICEMS)*, 616–619. https://doi.org/10.23919/icems.2018.8549478

[10] Gardouh, A. S., Abulanwar, S., Deng, F., Gouda, E., & Ghanem, A. (2025). Novel Unified Normalized DC Current-Based Diagnosis scheme of interturn and Open-Switch faults for VSI-FED induction motor drive system. *IEEE Transactions on Power Electronics*, *40*(10), 14710–14721. https://doi.org/10.1109/tpel.2025.3580295

[11] Bostanci, E., Moallem, M., Parsapour, A., & Fahimi, B. (2017). Opportunities and challenges of switched reluctance motor drives for electric propulsion: A comparative study. *IEEE Transactions on Transportation Electrification*, *3*(1), 58–75. https://doi.org/10.1109/tte.2017.2649883

[12] Abdel-Aziz, A., Elgenedy, M., & Williams, B. (2024). Review of switched reluctance motor converters and torque ripple minimisation techniques for electric vehicle applications. *Energies*, *17*(13), 3263. https://doi.org/10.3390/en17133263

[13] Son, I., Lukman, G. F., Shah, M. H., Jeong, K., & Ahn, J. (2021). Design considerations and selection of cost-effective switched reluctance drive for radiator cooling fans. *Electronics*, *10*(8), 917. https://doi.org/10.3390/electronics10080917

[14] Gopalakrishnan, S., Omekanda, A., & Lequesne, B. (2006). Classification and remediation of electrical faults in the switched reluctance drive. *IEEE Transactions on Industry Applications*, *42*(2), 479–486. https://doi.org/10.1109/tia.2006.870044

[15] Ali, N., & Narimani, M. (2024). Fault-tolerant SRM drives—A review. *IEEE Transactions on Power Electronics*, *39*(8), 10261–10275. https://doi.org/10.1109/tpel.2024.3392713

[16] Lorenz, F., Rudolph, J., & Werner, R. (2018). High Temperature Operation and Increased Cooling Capabilities of Switched Reluctance Machines using 3D Printed Ceramic Insulated Coils. *IEEE Transportation Electrification Conference and Expo*, 400–405. https://doi.org/10.1109/itec.2018.8450089

[17] Feng, L., Sun, X., Bramerdorfer, G., Zhu, Z., Cai, Y., Diao, K., & Chen, L. (2024). A review on control techniques of switched reluctance motors for performance improvement. *Renewable and Sustainable Energy Reviews*, *199*, 114454. https://doi.org/10.1016/j.rser.2024.114454

[18] Abdel-Aziz, A., Elgenedy, M., & Williams, B. (2024). A new torque control approach for torque ripple minimisation in switched reluctance drives. *Energies*, *17*(13), 3334. https://doi.org/10.3390/en17133334

[19] Kimpara, M. L. M., Reis, R. R. C., Da Silva, L. E. B., Pinto, J. O. P., & Fahimi, B. (2022). A two-step control approach for torque ripple and vibration reduction in switched reluctance motor drives. *IEEE Access*, *10*, 82106–82118. https://doi.org/10.1109/access.2022.3195493

[20] Lequesne, B., Gopalakrishnan, S., & Omekanda, A. M. (2005). Winding short circuits in the switched reluctance drive. *IEEE Transactions on Industry Applications*, *41*(5), 1178–1184. https://doi.org/10.1109/tia.2005.855051

[21] Gameiro, N. S., & Cardoso, A. J. M. (2012). A new method for power converter fault diagnosis in SRM drives. *IEEE Transactions on Industry Applications*, *48*(2), 653–662. https://doi.org/10.1109/tia.2011.2180876

[22] Marques, J. F., Estima, J. O., Gameiro, N. S., & Cardoso, A. J. M. (2014). A new diagnostic technique for real-time diagnosis of power converter faults in switched reluctance motor drives. *IEEE Transactions on Industry Applications*, *50*(3), 1854–1860. https://doi.org/10.1109/tia.2013.2279898

[23] Mollet, Y., Sarrazin, M., Van der Auweraer, H., & Gyselinck, J. (2018). Investigation of the influence of open-phase faults on noise and vibrations of switched reluctance machines. In *Proceedings of the 2018 IEEE International Conference on Industrial Technology (ICIT)*, Lyon, France, 20–22 February 2018. http://hdl.handle.net/2013/ULB-DIPOT:oai:dipot.ulb.ac.be:2013/268024

[24] Hu, Y., Gan, C., Cao, W., Zhang, J., Li, W., & Finney, S. J. (2016). Flexible fault-tolerant topology for switched reluctance motor drives. *IEEE Transactions on Power Electronics*, *31*(6), 4654–4668. https://doi.org/10.1109/tpel.2015.2477165

[25] Luo, P., Yin, Z., Zhang, Z., Zhang, Y., Zhang, P., & Liu, J. (2024). Diversified diagnosis strategy for PMSM inter-turn short-circuit fault via novel sliding mode observer. *IEEE Transactions on Power Electronics*, *39*(4), 4149–4159. https://doi.org/10.1109/tpel.2024.3352077

[26] Wang, B., Wang, J., Sen, B., Griffo, A., Sun, Z., & Chong, E. (2018). A fault-tolerant machine drive based on permanent magnet-assisted synchronous reluctance machine. *IEEE Transactions on Industry Applications*, *54*(2), 1349–1359. https://doi.org/10.1109/tia.2017.2781201

[27] Gardouh, A. S., Abulanwar, S., Deng, F., Gouda, E., & Ghanem, A. (2024). Novel fuzzy-based open-switch fault detection scheme of voltage source inverter induction motor drive. *IEEE Transactions on Power Electronics*, *39*(11), 14961–14973. https://doi.org/10.1109/tpel.2024.3438989

[28] Farah, N., Talib, M., Lazi, J., Ali, M. A., & Ibrahim, Z. (2017). Multilevel inverter fed switched reluctance motors (SRMs): 6/4, 8/6 and 10/8 SRM geometric types. *International Journal of Power Electronics and Drive Systems*, *8*(2), 584–592. https://doi.org/10.11591/ijpeds.v8.i2.pp584-592

[29] Zhang, K., Li, G. J., Zhu, Z. Q., & Jewell, G. W. (2019). Investigation on contribution of inductance harmonics to torque production in multiphase doubly salient synchronous reluctance machines. *IEEE Transactions on Magnetics*, *55*(4), 8101110. https://doi.org/10.1109/tmag.2019.2899803

[30] Mukhopadhyay, J., Choudhuri, S., & Sengupta, S. (2021). ANFIS based speed and current control with torque ripple minimization using hybrid SSD-SFO for switched reluctance motor. *Sustainable Energy Technologies and Assessments*, *49*, 101712. https://doi.org/10.1016/j.seta.2021.101712

[31] Hamouda, M., Menaem, A. A., Rezk, H., Ibrahim, M. N., & Számel, L. (2020). Numerical estimation of switched reluctance motor excitation parameters based on a simplified structure average torque control strategy for electric vehicles. *Mathematics*, *8*(8), 1213. https://doi.org/10.3390/math8081213

[32] Fang, G., Scalcon, F. P., Xiao, D., Vieira, R. P., Gründling, H. A., & Emadi, A. (2021). Advanced control of switched reluctance motors (SRMs): A review on current regulation, torque control and vibration suppression. *IEEE Open Journal of the Industrial Electronics Society*, *2*, 280–301. https://doi.org/10.1109/ojies.2021.3076807

[33] Siddiqui, K. M., Bonab, A. S., Shirinabadi, P., Ghavifekr, A. A., Kumar, S., Verma, S., & Gupta, S. (2025). Performance comparison of multi phase switched reluctance motors with varying pole configurations and power ratings. *i-manager's Journal on Circuits and Systems*, *13*(2), 14–23. https://doi.org/10.26634/jcir.13.2.22573

[34] Korkosz, M., Prokop, J., & Bogusz, P. (2024). The effect of the number of parallel winding paths on the fault tolerance of a switched reluctance motor. *Energies*, *17*(22), 5701. https://doi.org/10.3390/en17225701

[35] Son-In, S., Kulworawanichpong, T., & Pao-La-Or, P. (2020). Magnetic field comparison of 6/4 and 8/6 switched reluctance motor by using the 3-D finite element method. *International Journal of Smart Grid and Clean Energy*, *9*(1), 33–43. https://doi.org/10.12720/sgce.9.1.33-43

[36] Bieńkowski, K., Łapczyński, S., Szulborski, M., Kozarek, Ł., Gołota, K., Cichecki, H., Kolimas, Ł., Żelaziński, T., Smolarczyk, A., Babiński, A., & Owsiński, M. (2022). Validated analytical model of 8/6 and 10/8 switched reluctance motors. *Energies*, *15*(2), 630. https://doi.org/10.3390/en15020630